Published in final edited form as:
CrystEngComm. 2015 March 28; 17(12): 2504–2516. doi:10.1039/C5CE00118H.

Solid state forms of 4-aminoquinaldine - From void structures with and without solvent inclusion to close packing

Doris E. Braun[*,a], **Thomas Gelbrich**[a], **Volker Kahlenberg**[b], and **Ulrich J. Griesser**[a]

[a]Institute of Pharmacy, University of Innsbruck, Innrain 52c, 6020 Innsbruck, Austria.

[b]Institute of Mineralogy and Petrography, University of Innsbruck, Innrain 52, 6020 Innsbruck, Austria.

Abstract

Polymorphs of 4-aminoquinaldine (**4-AQ**) have been predicted in silico and experimentally identified and characterised. The two metastable forms, **AH** (anhydrate) **II** and **AH III**, crystallise in the trigonal space group $R\bar{3}$ and are less densely packed than the thermodynamically most stable phase **AH I°** ($P2_{1/c}$). **AH II** can crystallise and exist both, as a solvent inclusion compound and as an unsolvated phase. The third polymorph, **AH III**, is exclusively obtained by desolvation of a carbon tetrachloride solvate. Theoretical calculations correctly estimated the experimental 0K stability order, confirmed that **AH II** can exist without solvents, gave access to the **AH III** structure, and identified that there exists a subtle balance between close packing and number of hydrogen bonding interactions in the solid state of anhydrous **4-AQ**. Furthermore, the prevalence of void space and solvent inclusion in $R\bar{3}$ structures is discussed.

1. Introduction

Screening for different solid forms (polymorphs, hydrates, solvates) is an essential step during drug development.[1] This is because the crystal form dictates fundamental properties such as stability, solubility (bioavailability), mechanical properties, etc.,[2-4] and thus, suitable solid form(s) need to be identified and thoroughly characterised before they can be processed into high quality (drug) products. Controlling the solid state form is, therefore, of considerable interest since it provides a possibility to tune product properties without changing the chemistry of the molecule.[5] Solid form screens are typically attempted by crystallising the compound from a broad range of solvents or solvent mixtures under different conditions (e.g. rate of cooling, crystallisation temperature, solvent evaporation, precipitation with anti-solvent).[6-8] Templates, additives or impurities have been shown to result in the formation of new, sometimes otherwise elusive, solid forms,[9-12] making it practically not feasible to cover the whole range of techniques that may lead to alternate phases.[13]

Given this and the recent successes in computationally generating the crystal energy landscapes (crystal structure prediction, CSP),[13-28] in silico screening, might be used as an

---

[*] doris.braun@uibk.ac.at Tel: 0043 512 507 58653 .

assurance that all practically important forms have been found in an experimental screening programme, i.e. to minimise the risk of late-appearing crystal forms.[29] Based on the CSP results not only the propensity for polymorphism but also solvent inclusion (framework structures[30,31]), the potential for disorder[32,33] and local short-range order in the amorphous state[34] can be deduced. Another motivation for pursuing CSP studies is to increase the access to structural data. Finally, lattice energy estimations provide an alternative method to define the stability hierarchy of solid forms.[35,36]

During solvent crystallisation it can happen that solvent molecules co-crystallise with the host molecules, leading to the formation of solvates. The solvent molecules can simply fill channels or voids within the crystal lattice or interact with the host molecule through hydrogen bonding or other stabilising intermolecular interactions. The existence of a solvate depends on pressure, temperature, and amount of solvent present in the storage atmosphere.[37] Changes in the latter factors can induce a phase transformation to an alternative solid form (e.g., unsolvated crystalline phase, amorphous phase). When the solvent molecule becomes entrapped in the solid to some extent, in sub-stoichiometric amounts, and cannot be removed by suitable drying conditions the term “residual solvents” is used.[38] The solvent molecules are then considered as “impurities” and regulated by the ICH guideline Q3C (residual solvents in pharmaceuticals).[39] Probably the most famous example showing “solvent inclusion” (< 5 wt.%) is carbamazepine (CBZ) form II, where the solvent plays an important role in the crystallisation of the form II, by stabilising its crystal structure.[40,41]

The small organic molecule 4-aminoquinaldine (4-amino-2-methylquinolidine, **4-AQ**, Fig. 1) was subjected to a multidisciplinary solid form screening programme with the aim to contrast and evaluate experimental and computational search methods, as well as measured and computed energy differences between polymorphs. The investigated compound belongs to the pharmaceutically and biologically important class of quinolone derivatives and can be seen as a model compound for a co-crystal former. Surprisingly, hardly any information on solid forms of this compound can be found in the literature. Dimorphism of **4-AQ** has already been reported in 1969[42] and only the crystal structure of the monohydrate has been reported (Cambridge Structural Database[43] Refcode: LOBSOL[44]). In addition, experimental and computed Infrared and Raman spectra have been published by Krishnakumar and Xavier[45] and Arjunan et al.[46] The first of these reports gives the experimental spectral data for the anhydrate (**AH) I°**, and the second for the monohydrate. The water molecules have been ignored in these simulations.

The aim of this study was to develop a consistent picture of the solid state properties, structural and thermodynamic features of the three anhydrate polymorphs of **4-AQ** (including a novel phase) and its carbon tetrachloride solvate. This was possible only by combining of a broad range of analytical techniques (hot-stage microscopy, differential scanning calorimetry, thermogravimetric analysis, X-ray diffractometry and Infrared spectroscopy) complemented with crystal structure prediction.

2. Experimental Section

2.1. Materials and Solid Form Screen

4-AQ was purchased from Aldrich (Lot#STBD1705V, purity 98%). The substance was recrystallised for purification from a hot saturated ethanol solution at 8 °C. The 29 solvents used for the polymorphism screen were all of analytical quality and all organic solvents were purchased from Aldrich or Fluka.

The solid form screen encompassed a solvent crystallisation screening, sublimation and desolvation studies. The most commonly used solvents/solvent mixtures, covering different classes based on molecular descriptors (hydrogen bonding capability, polarity, dielectric constant and dipole moment) have been chosen.[47] Solvent evaporation, cooling crystallisation, anti-solvent addition and liquid assisted grinding experiments were employed for the solvent screening and are detailed in ESI† Section 1.1.

2.2. Infrared Spectroscopy (IR)

FT-IR spectra were recorded with a Bruker IFS 25 spectrometer connected to a Bruker IR microscope I with a 15x-Cassegrain-objective (Bruker Analytische Messtechnik GmbH, Ettlingen, Germany). The samples were prepared on ZnSe discs and the following measurement conditions were applied: spectral range 4000 to 600 cm^{-1}, resolution 4 cm^{-1}, 64 scans per spectrum.

2.3. X-ray Powder Diffractometry (XRPD)

The X-ray powder diffraction patterns were obtained using an X'Pert PRO diffractometer (PANalytical, Almelo, The Netherlands) equipped with a θ/θ coupled goniometer in transmission geometry, programmable XYZ stage with well plate holder, Cu-$K_{\alpha 1,2}$ radiation source with a focussing mirror, a 0.5° divergence slit and a 0.02° Soller slit collimator on the incident beam side, a 2 mm antiscattering slit and a 0.02° Soller slit collimator on the diffracted beam side and a solid state PIXcel detector. The patterns were recorded at a tube voltage of 40 kV, tube current of 40 mA, applying a step size of $2\theta = 0.013°$ with 80 s per step in the 2θ range between 2° and 40°.

2.4. Single Crystal X-ray Diffractometry

Single crystals of **AH I°** were obtained from sublimation experiments carried out between two glass slides, separated by a spacer ring of 5 mm thickness, on a Kofler hot bench at 130 °C. **AH II** crystals were prepared by slow solvent evaporation at 40 °C from a carbon tetrachloride solution saturated at room temperature. Essential crystal data are collected in Table 1. The data for **AH I°** (Mo radiation; $\lambda = 0.71073$ Å) were collected on a Rigaku AFC12 goniometer driven by the CrystalClear-SM Expert 3.1 b27 software (Rigaku, 2012) and equipped with an enhanced sensitivity (HG) Saturn724+ detector mounted at the window of an FR-E+ Super Bright Mo rotating anode generator with HFVarimax optics.[48]

[†] Electronic Supplementary Information (ESI) available: Conditions and outcomes of the manual solvent crystallisation screen; Pawley Fits, Infrared spectrum for S_{CCl4}; photographs; crystallographic information (cifs); potential energy surface scans; representation of the experimental structure; computationally generated AH crystal energy landscape; 2D Hirshfeld fingerprint plots for computed low energy structures; PIXEL energies. See DOI: 10.1039/b000000x/

The data for **AH II** (Mo radiation; λ = 0.71073 Å) were recorded on an Oxford Diffraction Gemini-R Ultra diffractometer operated by CrysAlis software.[49] The structures were solved by direct methods (SIR2011[50] or SHELXL2013[51]) and refined by full-matrix least squares on F^2 using SHELXL2013 and the program package WinGX.[52] Polar hydrogen atoms were located in difference maps, and those bonded to carbon atoms were fixed in idealised positions and their displacement parameters were set to 1.2*U*eq (for CH) or 1.5*U*eq (for the CH3 group) of the parent C atom, while the H atoms of the NH_2 group were refined freely. The hydrogen atoms in the $-CH_3$ group of **AH I°** were found to be statistically disordered over two positions with occupancies of 0.5:0.5 and of **AH II** with occupancies of 0.63:0.37 and 0.59:0.41, respectively.

2.5. Hot-stage Microscopy (HSM)

For hot-stage thermomicroscopic investigations a Reichert Thermovar polarisation microscope, equipped with a Kofler hot-stage (Reichert, A), was used. Photographs were taken with an Olympus DP71 digital camera (Olympus, D).

2.6. Differential Scanning Calorimetry (DSC)

DSC thermograms were recorded on a DSC 7 or Diamond DSC (Perkin-Elmer Norwalk, Ct., USA) controlled by the Pyris 7.0 software. Using a UM3 ultramicrobalance (Mettler, Greifensee, Switzerland), samples of approximately 2 - 6 mg were weighed into perforated or sealed aluminium pans. The samples were heated using rates in between 2 and 20 °C min^{-1}, with dry nitrogen as the purge gas (purge: 20 ml min^{-1}). The two instruments were calibrated for temperature with pure benzophenone (mp 48.0 °C) and caffeine (236.2 °C), and the energy calibration was performed with indium (mp 156.6 °C, heat of fusion 28.45 Jg^{-1}). The errors on the stated temperatures (extrapolated onset temperatures) and enthalpy values were calculated at the 95% confidence intervals (CI) and are based on at least five measurements.

2.7. Thermogravimetric Analysis (TGA)

TGA was carried out with a TGA7 system (Perkin-Elmer, Norwalk, CT, USA) using the Pyris 2.0 software. Approximately 2 - 5 mg of sample was weighed into a platinum pan. Two-point calibration of the temperature was performed with ferromagnetic materials (Alumel and Ni, Curie-point standards, Perkin-Elmer). Heating rates of 0.5 to 20 °C min^{-1} were applied and dry nitrogen was used as a purge gas (sample purge: 20 mL min^{-1}, balance purge: 40 mL min^{-1}).

2.8. Computational Generation of the Anhydrate Crystal Energy Landscape

The anhydrate crystal energy landscape was generated using the planar **4-AQ** molecule, obtained from the potential energy surface calculations with Gaussian09.[53] Using the program CrystalPredictor2.0,[54-56] 150,000 Z′=1 anhydrate structures were randomly generated in 48 space groups (ESI† Section 2.2.1) and 75,000 Z′=2 anhydrate structures in $R\bar{3}$ (chosen based on experimental evidence). Each crystal structure was relaxed to a local minimum in the intermolecular lattice energy, calculated from the FIT[57] *exp-6* repulsion-dispersion potential and atomic charges which had been fitted to electrostatic potential around the PBE0/6-31G(d,p) charge density using the CHELPG scheme.[58] All structures within 20 kJ mol^{-1} of the lowest energy structure (2520 Z′=1 and 390 Z′=2 structures) were reminimised using DMACRYS[59] with a more realistic, distributed multipole model[60] for the electrostatic forces which had been derived using GDMA2[61] to analyze the PBE0/6-31G(d,p) charge density.

The optimal proton positions of the amino group (i.e. pyramidal, deviation from planarity) and methyl group in all crystal structures within 15 kJ mol^{-1} of the global minimum (147 Z′=1 and 31 Z′=2 structures) were determined using the CrystalOptimizer database method.[62] This was done by minimising the lattice energy (E_{latt}), calculated as the sum of the intermolecular contribution (U_{inter}) and the conformational energy penalty paid for distortion of the molecular geometry to improve the hydrogen bonding geometries. Conformational energy penalties ($\Delta E_{\mathrm{intra}}$, with respect to the pyramidal global conformational energy minimum) and isolated molecule charge densities were computed at the PBE0/6-31G(d,p) level, for each conformation considered in the minimisation of E_{latt}.

The most stable structures (60 Z′=1 and 3 Z′=2 structures) were used as starting points for periodic electronic structure calculations. The DFT-D calculations were carried out with the CASTEP plane wave code[63] using the Perdew-Burke-Ernzerhof (PBE) generalized gradient approximation (GGA) exchange-correlation density functional[64] and ultrasoft pseudopotentials,[65] with the addition of a semi-empirical dispersion correction, either the Tkatchenko and Scheffler (TS)[66] or Grimme06 (G06)[67] model. For more details see ESI† Section 2.2.2.

PIXEL calculations[68-70] were also performed on the low energy structures to estimate the repulsive (E_R), dispersion (E_D), electrostatic (Coulombic, E_C) and polarisation (also called induction, E_P) contributions from individual pairs of molecules within a crystal. The charge density for the crystal was constructed from the MP2/6-31G(d,p) ab initio charge density of the isolated molecule as extracted from the computed PBE-TS crystal structure. The electron density was described using medium cube settings and a step size of 0.08 Å, with the pixels condensed into superpixels with a condensation level n=4.

3. Results

3.1. Solid Form Screening

The experimental screen for solid forms resulted in three anhydrate polymorphs (**AH I° – III**), a monohydrate (**MH**),[44] a carbon tetrachloride solvate (**S_{CCl4}**) and amorphous **4-AQ**. Either the **MH** or a mixture of **MH** and **AH I°** was obtained in the vast majority of evaporation experiments performed at room temperature (RT). **AH I°** was obtained from most experiments performed at 40 °C. **AH II** was formed in slow evaporation experiments from 1-butanol, carbon tetrachloride and tetrahydrofurane performed at 40 °C or concomitantly with **AH I°** from chloroform at RT. In addition, **S_{CCl4}/AH III** emerged from tetrachloride in room temperature evaporation experiments. From dimethyl formamide and dimethyl sulfoxide a different compound emerged at 40 °C which was not further characterised. Cooling crystallisation from different solvents or precipitation experiments with toluene or water resulted in **MH** or **AH I°** while **CCl_4** yielded **S_{CCl4}**. Depending on the water activity of the used solvent either **MH** or **AH I°** emerged from liquid assisted grinding experiments. For more details see ESI† Section 1.

Dehydration experiments starting from the **MH** resulted in **AH I°**, whereas desolvation of $\mathbf{S_{CCl4}}$ led to **AH III**. Finally, in sublimation experiments exclusively **AH I°** was obtained and recrystallisation form the melt at temperatures < 60 °C resulted in **AH II**.

3.2. Single Crystal Structures

The structures of **AH I°** and **AH II** (CCl_4), crystallised from carbon tetrachloride, were determined. The **4-AQ** molecule features only the aromatic amino group as a potential donor for two hydrogen bonds and the pyridine nitrogen as a hydrogen bond acceptor.

3.2.1. Anhydrate I°—This polymorph crystallises in the monoclinic space group $P2_{1/c}$ with Z′=1 (Table 1). The **4-AQ** molecule is essentially planar with the amino group adopting a slightly pyramidal conformation to optimise the geometry of the hydrogen bond. This is in contrast to the planar amino group in the monohydrate structure.[44] The **4-AQ** molecules are interlinked through N2–H2···N1 hydrogen bonds into a $C_2^1(6)$[71] chain motif, which propagates in direction of the *c* axis and exhibits glide plane symmetry (Fig. 2a). Hence, only one of the two polar protons is engaged in a strong intermolecular interaction. The $C_2^1(6)$ chains are stacked, forming π···π, along the crystallographic *a* axis. Adjacent stacks of $C_2^1(6)$ chains are related by inversion and linked through weak C–H···π contacts.

3.2.2. Anhydrate II—The second **4-AQ** polymorph crystallises in the trigonal space group $R\overline{3}$ with Z′=2 (Table 1). The single crystal structure data clearly revealed the presence of residual solvent, CCl_4, located in cavities. The solvent molecule is disordered around the $\overline{3}$ site at (0,0,0) and refined with the maximum possible occupancy of a **4-AQ**:CCl_4 ratio of 1:1/12. Similar to **AH I°** the **4-AQ** molecules are essentially planar with only one amino proton deviating slightly from the plane defined of the aromatic ring system. Three distinct hydrogen bonded ring motifs involving both independent **4-AQ** molecules can be identified, i.e. $R_4^2(8)$ forming a tetrameric, $R_6^6(36)$ forming a hexameric, and $R_{12}^{12}(72)$ forming a 12-membered **4-AQ** ring motif. The two symmetry independent **4AQ** molecules are denoted A and B hereafter. The two polar protons of molecule A are engaged in N_A–H···N_B hydrogen bonds to the pyridine N1 of molecule B. Only one of the polar protons of molecule B forms a strong hydrogen bond, N_B–H2···N_A, to the pyridine N1 of molecule A. The $R_4^2(8)$ ring motif is formed by the two N_A–H1/2···N_B hydrogen bonds. Alternating N_A–H1···N_B and N_B–H2···N_A hydrogen bonds form the hexameric ring motif and alternating N_A–H2···N_B and N_B–H2···N_A hydrogen bonds the 12-membered hydrogen bonded ring. Thus, in contrast to the **AH I°** structure, three of the four N–H protons are involved in strong intermolecular interactions. Altogether, the **4-AQ** molecules form hydrogen bonded layers, which lay parallel to the *ab*-plane (Fig. 3a). Layers of this kind are related by inversion, leading to voids around the roto-inversion axes (Fig. 3b and c). The hydrophobic cavities can accommodate solvent molecules (Fig. 3d), but no strong intermolecular interactions are formed between the host and guest molecules. Thus, the solvent molecules only fill the structural voids. In addition, C–H···π interactions stabilise **AH II**.

3.2.3. Monohydrate—The **MH** structure[44] has the space group symmetry $Pna2_1$, with Z′ = 1. The structure is densely packed and all hydrogen bonding donor and acceptor groups are involved in strong intermolecular interactions. A further characteristics of the structure are $\pi \cdots \pi$ of **4-AQ** molecules.

3.3. Identification and Characterisation of 4-AQ Anhydrates and Carbon Tetrachloride Solvate

3.3.1. Fourier Transform Infrared Spectroscopy—The **4-AQ MH**, **AH I°**, **AH III** and $\mathbf{S_{CCl4}}$ forms showed high reproducibility in their analytical data. In contrast, **AH II**, obtained using different crystallisation conditions, i.e the melt [**AH II** (melt)] or different solvents [(**AH II** (CCl_4) and **AH II**($CHCl_3$)], showed variability in its spectral, X-ray diffraction and thermo-analytical data. Exemplarily, the FT-IR spectra of the three anhydrates, including different **AH II** batches, are given in Fig. 4 and selected IR band positions are listed in Table 2. The three anhydrates can be easily distinguished based on their νNH_2 and νCH stretching vibrations. Furthermore, the δNH_2 and δCH_3 band positions can be used to identify the phases. **AH II** is likely to be a Z′=2 phase for **AH II** (νNH_2 bands split for **AH II**) and **AH I°** and **AH III** Z′=1 phases.

A closer analysis was necessary for **AH II** (which will be discussed later). Figure 4b contrasts three different **AH II** samples, which were crystallised either from the melt, carbon tetrachloride or chloroform. Overall, their IR spectra are similar but show distinguishable features in the νCH_3 and δCH_3 region, in particular between **AH II** (melt) on the one hand and **AH II** (CCl_4) and **AH II**(CCl_4) on the other hand. Band positions within the fingerprint region do not differ (beyond the resolution of the instrument) with the exception of the regions of νCCl vibrations (840 – 740 cm^{-1}). Nevertheless, based on the similarity of the IR spectra (Figure 4b) it can be suggested that all three crystallisation products are the same solid form and solvent molecules are located beside apolar protons in **AH II** (CCl_4) **and AH II** (CCl_3). All **4-AQ** intermolecular interactions can be expected to be the same from the spectroscopic **AH II** data.

3.3.2. X-ray Powder Diffraction—The XRPD patterns of the **AH II** samples crystallised from the melt or from a solution differ only slightly in their peak positions but significantly in the intensities of their low-angle reflections (Fig. 5). Pawley fits of the different **AH II** samples, using the cell information of **AH II** (CCl_4), confirmed the same space group symmetry, $R\overline{3}$, with similar lattice parameters (ESI† Figures S3-S5). Peak shifts can be attributed to small changes in lattice parameters (Δa and $\Delta c < 0.5\%$) and differences in intensities may be related to additional residual solvent (see section 3.4.2).

The XRPD patterns of $\mathbf{S_{CCl4}}$ and its desolvation product **AH III** show some resemblance as well, despite significant changes in peak positions and intensities. This may imply a structural relationship between the two phases which could explain why **AH III** was only obtained from desolvation of $\mathbf{S_{CCl4}}$ (see section 3.5.3).

3.4. Thermal Characterisation

3.4.1. Solvent-Free Forms: Anhydrates I° – III and amorphous 4-AQ—The anhydrate polymorphs were analysed with DSC (Fig. 6a) and HSM (Fig. 6b). The DSC curve of **AH I°** shows only one thermal event, the melting, which occurs at 167.3 ± 0.1 °C (onset temperature) with an enthalpy of fusion, $\Delta_{fus}H_{I°}$, of 25.4 ± 0.1 kJ mol^{-1} (Table 3). Similarly, the DSC trace of **AH III** shows one event, melting at 157.1 ± 0.3 °C (onset temperature) with $\Delta_{fus}H_{III}$ of 20.0 ± 0.5 kJ mol^{-1}. Quench cooling of the melt results in amorphous **4-AQ**. The glass transition of the latter phase is observed around room temperature (25 °C) and spontaneous nucleation of **AH II** (Fig. 6b, first picture) occurs at temperatures > 45 °C. Upon further heating of **AH II**, an exothermic phase transformation to **AH I°** occurs between 100 and 140 °C, which can also clearly be seen with HSM (Fig. 6b, second and third photograph) and indicates a monotropic relationship between **AH I°** and **AH II**. The HSM observations are essentially in agreement with the descriptions given by Kofler and Kolsek.[42] The transition enthalpy, $\Delta_{trs}H_{II\text{-}I°}$, was determined by us to be –3.3 ± 0.1 kJ mol^{-1}. The final event in the DSC curve (Fig. 6a, second curve) corresponds to the melting of **AH I°**. Concomitant nucleation of forms **AH I°** and **AH II** is observed when the melt is annealed at temperatures ≥ 70 ° C. If **AH II** is contaminated with **AH I°**, the solid-solid phase transformation is accelerated and occurs within days at room conditions. Furthermore, the HSM investigations revealed strong sublimation of **4-AQ**, with the sublimed plate-shaped crystals being **AH I°** (ESI† Figure S1).

3.4.2. Solvent Containing Forms: Anhydrate II and Carbon tetrachloride Solvate—Thermal analytical techniques have provided experimental evidence for solvent inclusion in **AH II**. The release of solvent can be observed by heating a sample immersed in high viscosity silicon oil. DSC traces exhibit a small endothermic event around 120 °C (not shown in Fig. 6), within the temperature range of the **AH II** → **AH I°** phase transition. The observation of an endothermic rather than an exothermic event can be interpreted in terms of an expulsion of solvent molecules. The TGA curves of **AH II** crystallised from solution reveal a clear mass loss of 4.5 – 6% prior to sublimation, depending on the nature of the solvent (Fig. 7a). The measured mass loss corresponds to substoichiometric ratios, e.g. ~1/12 mol of carbon tetrachloride or 1-butanol per mol **4-AQ**. The melt crystallised **AH II** sample shows no mass loss except for sublimation at temperatures > 130 °C.

It was not possible to “desolvate” the solvent containing **AH II** samples to produce solvent-free **AH II**. The release of the solvent molecules always resulted in the destruction of the crystal lattice. Thus, it was concluded that solvent molecules were entrapped at isolated sites of the **AH II** structure during crystallisation and are not freely accessible anymore once the crystals are formed.

The $\mathbf{S_{CCl4}}$ solvate is unstable and desolvation to **AH III** is completed within days at ambient conditions. Exposure to the lowest relative humidity (RH) levels leads to a fast desolvation at room temperature with the appearance of cracks and darkening of the crystals in non-polarised light. The measured mass loss of 15.6 ± 0.7% derived from TGA (Fig. 7a) corresponds to 0.19 ± 0.01 mol of carbon tetrachloride per mol of **4-AQ**.

3.5. Crystal Energy Landscape

The experimental forms **AH I°** and **AH II** correspond to the lowest and second lowest energy structures on the crystal energy landscape (Fig. 8), with rmsd_{15} values of 0.22 Å and 0.19 Å for **AH I°** and **AH II**, respectively (ESI† Table S7). The combination of the applied search routine and lattice energy minimisation method produced a sufficiently realistic crystal energy landscape. This allowed the complementary interpretation of the experimental results using the computed low energy structures. All structures within 10 kJ mol^{-1} of the global minimum, 19 structures, were used for interpreting the possible **4-AQ** solid form diversity.

3.5.1. Structural Diversity on the Crystal Energy Landscape—The computationally generated **4-AQ** structures (Fig. 8) exhibit a planar conformation with the C–C–N2–H1/2 dihedrals deviating by less than 25° from the plane of the aromatic rings. Thus, the structures differ solely in their packing arrangements and can be seen as (hypothetical) “packing polymorphs”.[72] As expected, only two distinct hydrogen bonding interactions are formed among the computed structures, N2–H1⋯N1 and N2–H2⋯N1, respectively. Due to the molecular geometry of **4-AQ** and the range of possible symmetry operations only one of the donor groups can be engaged in hydrogen bonding in $Z'=1$ structures. In case of a $Z'=2$ structure it is possible that both amino protons form hydrogen bonds (Fig. 3a, molecule A), although at cost of close packing (**AH II** on Fig. 8a). Using the H2 as a donor allows more packing possibilities amongst the most stable structures, 13 of the lowest structures form N2–H2⋯N1 hydrogen bonds, three N2–H1⋯N1, and only one shows both types. The global minimum structure, **AH I°**, shows the N2–H2⋯N1 connectivity, the second lowest structure, **AH II**, both possibilities and the fourth lowest energy structure is the most stable structure with a N2–H1⋯N1 hydrogen bond. In addition to the hydrogen bonds also C–H⋯π and π⋯π close contacts (Fig. 9) are essential for the stability of the **4-AQ** structures (ESI† Table S8).

3.5.2. Void Space Analysis—A striking feature of Fig. 8a is the broad range of packing indices among the most stable structures, spanning 67.4 to 77.5 %. Analyzing the void space of the computationally generated structures revealed that eight of the 19 most stable structures are not densely packed, with some of the structures showing significant void space (Fig. 8b). Amongst those structures are the solvent-free **AH II** and **AH III,** the fourth lowest energy structure (Fig. 9b and d).

3.5.3. Proposed Anhydrate III Structure—AH III, estimated to be 5.4 ± 0.6 kJ mol^{-1} less stable than **AH I°** (Table 3), was obtained exclusively by desolvating $\mathbf{S_{CCl4}}$. Only a low crystallinity product was observed, which did not allow us to solve the structure from X-ray powder diffraction data. The experimental XRPD data indexed to a trigonal unit cell (a = 31.511(4) Å, c = 4.6658(8) Å) and space group $R\bar{3}$ using the first 20 peaks with DICVOL04 on statistical assessment of systematic absences[75] and the DASH[76] and Topas Academic V5[77] packages. IR spectroscopy indicated the presence of a $Z' = 1$ structure (Fig. 4). By comparing the experimental XRPD pattern to the simulated powder patterns of the computationally generated low energy structures (Fig. 8) it should be possible to identify **AH III**. The experimental XRPD pattern of **AH III** matches the pattern simulated from the fourth most stable structure ($R\overline{3}$, Z′ = 1, a = 32.265 Å, c = 4.425 Å). Equally, the experimental **AH I°** and **AH II** XRPD patterns match with those simulated from the corresponding computationally derived structures. Thus, the fourth lowest energy structure corresponds to **AH III**.

In **AH III** the **4-AQ** molecules form a hydrogen bonded $R_6^6(36)$ ring motif mediated through N2–H1···N1 interactions and roto-inversion symmetry (Fig. 10a). Adjacent $R_6^6(36)$ rings interact through C–H···π intermolecular interactions (Fig. 9c) and are stacked in direction of the c axis. The **AH III** structure shows significant void space (Fig. 8b), which is located in hydrophobic channels in direction of the c axis (Fig. 10). The occurrence of a channel structure agrees with the fact that **AH III** is observed on route of desolvation. The XRPD patterns of **AH III** and $\mathbf{S_{CCl4}}$ show resemblance. Distinct shifts to lower diffraction angles of the peak positions in $\mathbf{S_{CCl4}}$ (Fig. 5) imply, as expected, a bigger unit cell for the solvate. Changes in diffraction intensities of the peaks, in particular $(2\overline{1}0)$, on which the roto-inversion axis is located in **AH III**, may indicate the presence of CCl_4 along the $\overline{3}$ axis in $\mathbf{S_{CCl4}}$ if the space group is maintained. Based on the IR spectra of $\mathbf{S_{CCl4}}$ and **AH III** we can exclude isostructurality as there are significant differences in the region of the νNH_2 and νCH stretching vibrations (ESI† Figure S9). This is also supported by the HSM investigations which showed darkening of the crystals ("pseudomorphosis" [78]) rather than only the appearance of cracks on the surfaces of the crystals. Thus, **AH III** and $\mathbf{S_{CCl4}}$ may belong to the same crystal system, which would facilitate a phase transformation, but differ in packing (hydrogen bonding). The $R_6^6(36)$ rings motif of the **AH III** structure may only be accessible via the $\mathbf{S_{CCl4}}$.

Overall, the experimental **4-AQ** structures, **AH I°-III** and **MH**, show very little structural similarity to each other. The only common building block is a one-dimensional stack of **4-AQ** molecules, which is present in **AH I**, **AH III** and **MH**.

3.6. Thermodynamic and Kinetic Stability of 4-AQ Anhydrates

The DSC and slurry experiments of the three anhydrates revealed that **AH I°** is the thermodynamically most stable polymorph. Since **AH I°** melts at a higher temperature and shows a higher enthalpy of fusion (Table 3) than **AH III** the two polymorphs are monotropically related.[79] The transformation of **AH III** to **AH I°** occurs within days at RT. Similarly, **AH II** is metastable relative to **AH I°** and from the exothermic transition to the stable form between 100 and 140 °C (see Fig. 6) we can also conclude that **AH II**/**AH I°** is a monotropic pair of polymorphs. Phase pure solvent-free **AH II** transforms within two to three weeks to **AH I°** at RT and much faster at higher temperatures (Fig. 6b). In contrast, **AH II** samples obtained by solvent crystallisation are more stable than the solvent-free **AH II** samples but still transform to **AH I°** and **MH** within less than a year if stored at room conditions. Transformation to the **MH** was observed for all polymorphs if stored at RH values above 40 % RH.

The thermodynamic stability order at 0 K was determined to be **AH I°** (most stable) > **AH II** > **AH III** (least stable). The experimental energy differences between the three polymorphs, derived from the heat of fusion ($\Delta_{fus}H$) and transformation ($\Delta_{trs}H$) enthalpies, were measured as 3.3 ± 0.1 kJ mol^{-1} between **AH I°** and **AH II** and 5.4 ± 0.6 kJ mol^{-1} between **AH I°** and **AH III** (Table 3). These experimental values agree well with the 0 K lattice energies differences of 3.2 and 4.8 kJ mol^{-1} for **AH I°/II** and **AH I°/III**, respectively. The presence of a Z′=2 anhydrate and solvent inclusion may explain why the more stable **AH II** shows a lower density than the less stable **AH III,** which represents an exception to the density rule.[79]

4. Discussion

4.1. Solvent Inclusion in $R\overline{3}$ Structures

The best known example of a solid form crystallising in $R\overline{3}$ and showing solvent inclusion is carbamazepine (CBZ) form II.[40,41] The resemblance in solid state behaviour of the two phases, CBZ form II and **4-AQ AH II**, and the fact that all $R\overline{3}$ structures on Fig. 8 show considerable void space inspired us to closer investigate the occurrence of solvate formation/void space in known $R\overline{3}$ structures present in the Cambridge Structural Database[43] (CSD). A search for $R\overline{3}$ structures containing only C, N, O and H atoms revealed that more than half of the structures (56%) have a guest molecule on the $\overline{3}$ axis, with the solvent molecule either modelled or residual electron density noted by the authors who could not model the solvent molecule. The remaining 44% of the 203 unique CSD structures exhibit either a symmetric molecule on the $\overline{3}$ axis or (considerable) void space, which was not commented on by the authors. These results agree with the CSD survey performed earlier by Fabbiani et al.[40] The void space around the roto-inversion axis can either show the features of isolated sites, e.g. Fig. 3b&c, or channels, e.g. Fig. 10. The shape of the void space will strongly influence the stability and characteristics of the solid from. In both cases the solvent molecules may be necessary for the formation of the structure, i.e. act as a template. In case of a channel structure, the solvent content can depend on the environmental conditions and it may even be possible to exchange the guest molecules without major rearrangements of the structure. This is in contrast to the isolated void site structures where normally the guest molecule can only be released in a destructive mechanism, which results in a distinct solid form exhibiting different properties. Either type can cause practical problems. The problems with substoichiometric solvent inclusions are well known and regulated for pharmaceuticals under the term “residual solvents”.[39]

4.2. 4-AQ AH II and Carbamazepine Form II

Despite the similarities of the two solid state phases, forms II of CBZ and **4-AQ**, they show distinct characteristics. Firstly, **4-AQ AH II** is to our knowledge the only example where solvent molecules (carbon tetrachloride, chloroform, tetrahydrofurane, 1-butanol) can be entrapped in the structure of **AH II.** However, their presence is not necessary for the nucleation and growth of this phase, as evidenced by the melt film crystallisation of **AH II**. This ascertainment is supported by the computationally generated anhydrate crystal energy landscape, which revealed **AH II** as the second lowest energy structure only 3 kJ mol^{-1} above the global minimum. In the case of CBZ form II was found on the corresponding CBZ crystal energy landscape, albeit higher in energy.[80,81] Cruz-Cabeza et al. rationalised that the computed high energy structure corresponds to the CBZ form II framework and that solvent inclusion stabilises this phase.[41] However, the inclusion of solvent molecules also seems to increase the barrier for the **AH II** to **AH I°** phase transformation in **4-AQ**, i.e. **AH II** samples containing residual solvent were stable for a longer time than solvent-free **AH II** samples (see section 3.6). The two phases differ considerably in their overall stability. The investigation of 25 years old in house samples of CBZ II (containing carbon tetrachloride, toluene, butanol or ethyl acetate as guest molecules) revealed that only a part of the sample transformed to CBZ form III after this long storing time at ambient conditions. In contrast, all **4-AQ AH II** samples transformed to **AH I°** after storing the sample under the same conditions for only 18 months.

4.3. Carbon Tetrachloride Solvate as an Intermediate Phase for Producing AH III

The formation of a specific solvate form may be the only route to an otherwise elusive phase, e.g. premofloxacin,[82] cinacalect HCl,[83] prilocaine HCl,[84] DB7 (3-(4-dibenzo[b,f][1,4]oxepin-11-yl-piperazin-1-yl)-2,2-dimethylpropanoic acid).[27] Thus, the formation of solvates not only expands the solid form landscape of a compound but also the possible screening techniques, i.e. desolvation studies, as recently discussed for two model pharmaceuticals.[27] The awareness of the occurrence of solvent adducts, as **4-AQ** $\mathbf{S_{CCl4}}$, increased immensely over the last decade. Solvate formation is rather common among organic (drug) molecules as shown by the steadily growing number of scientific publications and patent applications dealing with this topic. The formation of a highly unstable intermediate solvates can be easily overlooked, especially if the analytics is not performed on “wet” but dried samples. This then can lead to incorrect conclusions about the influence of the solvent on the nucleation of a specific solid form and our general understanding about templating effects.

The **4-AQ** $\mathbf{S_{CCl4}}$ can be seen as both, an intermediate solvate form and, to our knowledge, as the only gateway to **AH III**. This solvate seems to be the necessary precursor for the formation of the N2–H1···N1 hydrogen bonded $R_6^6(36)$ ring motifs, preventing the formation of the close packed $C_2^1(6)$ chain motif found for **4-AQ** which would be otherwise preferred. In contrast to examples with flexible molecules,[85] the solvate formation of **4-AQ** cannot be ascribed to the inability of its molecules to pack efficiently, but may be interpreted as a possibility to expand the observed hydrogen bonding and packing motifs. The presence of carbon tetrachloride does not automatically lead to the formation of the solvate, but the degree of supersaturation and the crystallisation temperature determine whether $\mathbf{S_{CCl4}}$ or **AH II** (CCl_4) is formed. The solvate crystallises preferentially from supersaturated solutions and at room temperature, as indicated by TGA experiments (Fig. 7a).

4.4. Computational and Experimental Solid Form Screening

The interpretation of computationally generated low energy structures can provide information about possible and energetically feasible intermolecular interactions and packing arrangements in a compound, which would not be accessible from experiments. The lattice energy, often in combination with the packing index/density, is normally used to select the most likely alternative structures. In the case of **4-AQ**, Fig. 8 clearly indicates that packing efficiency/density does not directly correlate with stability. The molecular shape of **4-AQ** dictates that a close packing can be achieved, but with only half of the hydrogen bonding donors involved in strong intermolecular interactions. The number of hydrogen bonding interactions can be increased by increasing the number of independent **4-AQ** molecules (cf., **AH II**), but at the cost of packing efficiency. By adding additional H-bonding acceptor/donor groups, as in **MH** (LOBSOL),[44] the frustration between packing efficiency and number of strong intermolecular interactions is resolved. Thus, for solvent-free **4-AQ** forms there is a subtle balance between close packing and the number of strong intermolecular interactions (i.e. hydrogen bonds). Furthermore, the planarity of the aromatic **4-AQ** molecule favours the formation of π···π or C–H···π interactions, which significantly contribute to the lattice energy of every structure on Fig. 8 (ESI† Table S8).

Crystal energy landscapes can guide experimental investigations to find alternative polymorphs, as demonstrated for CBZ form V[11] or creatine.[28] When one considers the outcome of the crystal structure predictions illustrated in Fig. 8, which reproduces the structures and stability order of the experimental forms reasonably well, it appears not to be unlikely that additional **4-AQ** polymorphs can be generated experimentally. The third (**3**, ESI† Table S6), fifth (**5**) and sixth (**6**) lowest energy structures are still within 6 kJ mol^{-1} of **AH I°**, and based on energy, the most probable candidates when the effects of thermal motion are neglected. Structures **3** and **6** show no packing similarity[86] with the experimental polymorphs. The strongest intermolecular interactions are in both cases the $C_2^1(6)$ hydrogen bonded chains involving either H2 (**3**) or H1 (**6** as a donor. Nucleation of **3** would require an environment that prevents the formation of π···π interactions, as in the more stable packing **AH II**. In **6** π···π interactions strongly contribute to the stability of the structure (ESI† Figure S14b), as in **AH III**, the polymorph showing the same N2–H1···N1 hydrogen bonding connectivity. One could assume that the right crystallisation conditions for those forms have not been found/applied yet. However, both hypothetical structures may not have enough void space to be templated by solvent molecules. Structure **5** shows packing similarity with **AH I°**. The two structures are built up of the same π···π stacked $C_2^1(6)$ chain motifs, differing only slightly in the stacking of the 2D building blocks, the C–H···π/C short contacts. With **AH I°** being the thermodynamically most stable form (as experimentally confirmed), structure **5** is unlikely to be observed as a long-lived metastable polymorph as its transformation to **AH I°** would be facile.

The combination of experimental and computational results gives us reassurance that **AH I°** is the thermodynamically most stable form, and that low density structures play a crucial role in the solid form landscape of **4-AQ**.

5. Conclusions

Crystal structure prediction for a small organic model compound, 4-aminoquinaldine, was successfully performed as part of an interdisciplinary study. The computationally generated anhydrate crystal energy landscape provided insight into the range of possible and stable packing arrangements and explained the unique solid state behaviour of **4-AQ**. The complex crystallisation behaviour of this compound is determined by the interplay between dense packing and a number of possible strong intermolecular interactions (hydrogen bonds).

Analysing the void space of the computed structures rationalised the solvent inclusion behaviour.

The thermodynamically most stable anhydrate, **AH I°**, a densely packed structure, was found as the global minimum of the computed crystal energy landscape. The two metastable forms, **AH II** and **AH III** (both $R\bar{3}$), were amongst the lowest energy structures (ΔE_{latt} relative to **AH I°** < 5 kJ mol^{-1}), rank two and four, respectively, but showed both considerable void space. The solvent accessible volume accounts for the fact that the formation of the metastable anhydrates can be templated by solvent inclusion. The isolated void space present in **AH II** can be filled either with solvent molecules (4.5 – 6 wt.%), or, in contrast to other known examples showing solvent inclusion in structural voids, be empty. The presence of the solvent molecules is not essential for the formation of this phase but contributes to the stability of **AH II**, i.e. slow down the phase transformation to **AH I°**. The third polymorph, **AH III**, was exclusively obtained by desolvating the carbon tetrachloride solvate and exhibits void space in channels. Its structural information could be derived by comparing the experimental X-ray powder diffraction pattern to simulated patterns of the computationally generated anhydrate structures. Based on the structural features the role of the solvate as a precursor is rationalised.

As demonstrated in this study, carefully conducted CSP can help to understand the complexity of the solid form landscape of a molecule. Analysing void space has been shown to be a useful tool for identifying phases that might be templated or stabilised by solvent inclusion.[41] We think that studies like this will help to advance computational methodologies for predicting thermodynamically feasible crystal structures and identifying putative alternative polymorphs.

Supplementary Material

Refer to Web version on PubMed Central for supplementary material.

Acknowledgements

The authors are grateful to Profs. C. C. Pantelides and C. S. Adjiman (Imperial College London) for the use of the CrystalPredictor and CrystalOptimizer programs, to Prof. S. L. Price (University College London) for the use of the DMACRYS program, and to V. Illing for experimental assistance. DEB gratefully acknowledges funding by the Hertha Firnberg Programme of the Austrian Science Fund (FWF, project T593-N19). This work was supported by the Austrian Ministry of Science BMWF as part of the UniInfrastrukturprogramm of the Focal Point Scientific Computing at the University of Innsbruck.

Notes and references

1. Brittain , HG. Polymorph in Pharmaceutical Solids. Brittain , HG., editor. Informa Healthcare; 2009. p. 1
2. Hilfiker, R. Polymorphism: In the Pharmaceutical Industry. Wiley-VCH; Germany: 2006.
3. Bernstein, J. Polymorphism in Molecular Crystals. Clarendon Press; Oxford: 2002.
4. Byrn , SR.; Pfeiffer , RR.; Stowell , JG. Solid-State Chemistry of Drugs. 2. SSCI, Inc.; West Lafayette, Indiana: 1999.
5. Bernardes CES, da Piedade MEM. Cryst. Growth Des. 2012; 12:2932–2941.
6. Llinas A, Goodman JM. Drug Discover. Today. 2008; 13:198–210.

7. Aaltonen J, Alleso M, Mirza S, Koradia V, Gordon KC, Rantanen J. Eur. J. Pharm. Biopharm. 2009; 71:23–37. [PubMed: 18715549]
8. Florence AJ, Johnston A, Fernandes P, Shankland N, Shankland K. J. Appl. Crystallogr. 2006; 39:922–924.
9. Zencirci N, Gelbrich T, Kahlenberg V, Griesser UJ. Cryst. Growth Des. 2009; 9:3444–3456.
10. Stokes SP, Seaton CC, Eccles KS, Maguire AR, Lawrence SE. Cryst. Growth Des. 2014; 14:1158–1166.
11. Arlin JB, Price LS, Price SL, Florence AJ. Chem. Commun. 2011; 47:7074–7076.
12. Eccles KS, Deasy RE, Fabian L, Braun DE, Maguire AR, Lawrence SE. CrystEngComm. 2011; 13:6923–6925.
13. Braun DE, Karamertzanis PG, Arlin JB, Florence AJ, Kahlenberg V, Tocher DA, Griesser UJ, Price SL. Cryst. Growth Des. 2011; 11:210–220.
14. Braun DE, Bhardwaj RM, Florence AJ, Tocher DA, Price SL. Cryst. Growth Des. 2013; 13:19–23.
15. Stephenson GA, Kendrick J, Wolfangel C, Leusen FJ. Cryst. Growth Des. 2012; 12:3964–3976.
16. Kendrick J, Stephenson GA, Neumann MA, Leusen FJ. Cryst. Growth Des. 2013; 13:581–589.
17. Gorbitz CH, Dalhus B, Day GM. Phys. Chem. Chem. Phys. 2010; 12:8466–8477. [PubMed: 20461256]
18. Braun DE, Ardid-Candel M, D'Oria E, Karamertzanis PG, Arlin JB, Florence AJ, Jones AG, Price SL. Cryst. Growth Des. 2011; 11:5659–5669.
19. Braun DE, Bhardwaj RM, Arlin JB, Florence AJ, Kahlenberg V, Griesser UJ, Tocher DA, Price SL. Cryst. Growth Des. 2013; 13:4071–4083.
20. Braun DE, Karamertzanis PG, Price SL. Chem. Commun. 2011; 47:5443–5445.
21. Cruz-Cabeza AJ, Day GM, Jones W. Chem. Eur. J. 2008; 14:8830–8836. [PubMed: 18752227]
22. Cruz-Cabeza AJ, Karki S, Fabian L, Friscic T, Day GM, Jones W. Chem. Commun. 2010; 46:2224–2226.
23. Bardwell DA, Adjiman CS, Arnautova YA, Bartashevich E, Boerrigter SX, Braun DE, Cruz-Cabeza AJ, Day GM, la Valle RG, Desiraju GR, van Eijck BP, Facelli JC, Ferraro MB, Grillo D, Habgood M, Hofmann DW, Hofmann F, Jose K, V, Karamertzanis PG, Kazantsev AV, Kendrick J, Kuleshova LN, Leusen FJ, Maleev AV, Misquitta AJ, Mohamed S, Needs RJ, Neumann MA, Nikylov D, Orendt AM, Pal R, Pantelides CC, Pickard CJ, Price LS, Price SL, Scheraga HA, van de Streek J, Thakur TS, Tiwari S, Venuti E, Zhitkov IK. Acta Crystallogr., Sect. B. 2011; 67:535–551. [PubMed: 22101543]
24. Kazantsev AV, Karamertzanis PG, Adjiman CS, Pantelides CC, Price SL, Galek PT, Day GM, Cruz-Cabeza AJ. Int. J. Pharm. 2011; 418:168–178. [PubMed: 21497184]
25. Bhardwaj RM, Price LS, Price SL, Reutzel-Edens SM, Miller GJ, Oswald IDH, Johnston B, Florence AJ. Cryst. Growth Des. 2013; 13:1602–1617.
26. Ismail SZ, Anderton CL, Copley RC, Price LS, Price SL. Cryst. Growth Des. 2013; 13:2396–2406.
27. Braun DE, McMahon JA, Koztecki LH, Price SL, Reutzel-Edens SM. Cryst. Growth Des. 2014; 14:2056–2072.
28. Braun DE, Orlova M, Griesser UJ. Cryst. Growth Des. 2014; 14:4895–4900.
29. Chemburkar SR, Bauer J, Deming K, Spiwek H, Patel K, Morris J, Henry R, Spanton S, Dziki W, Porter W, Quick J, Bauer P, Donaubauer J, Narayanan BA, Soldani M, Riley D, McFarland K. Org. Process Res. Dev. 2000; 4:413–417.
30. Cruz-Cabeza AJ, Day GM, Jones W. Chem. -Eur. J. 2009; 15:13033–13040. [PubMed: 19876969]
31. Pyzer-Knapp EO, Thompson HPG, Schiffmann F, Jelfs KE, Chong SY, Little MA, Cooper AI, Day GM. Chem. Sci. 2014; 5:2235–2245.
32. Copley RCB, Barnett SA, Karamertzanis PG, Harris KDM, Kariuki BM, Xu MC, Nickels EA, Lancaster RW, Price SL. Cryst. Growth Des. 2008; 8:3474–3481.
33. Braun DE, Tocher DA, Price SL, Griesser UJ. J. Phys. Chem. B. 2012; 116:3961–3972. [PubMed: 22390190]
34. Habgood M, Lancaster RW, Gateshki M, Kenwright AM. Cryst. Growth Des. 2013; 13:1771–1779.
35. Gelbrich T, Braun DE, Ellern A, Griesser UJ. Cryst. Growth Des. 2013; 13:1206–1217.

36. Braun DE, Gelbrich T, Kahlenberg V, Griesser UJ. Mol.Pharmaceutics. 2014; 11:3145–3163.
37. Bernardes CES, Piedade MF, Minas da Piedade ME. Cryst. Growth Des. 2010; 10:3070–3076.
38. Griesser, UJ. Polymorphism: In the Pharmaceutical Industry. Hilfiker, Rolf, editor. Wiley-VCH; Germany: 2006. p. 211-233.
39. ICH Q3C Impurities: *Guideline for Residual Solvents*. International Conference on Harmonization of Technical Requirements for Registration of Pharmaceuticals for Human Use; Geneva, Switzerland. 1997;
40. Fabbiani FPA, Byrne LT, McKinnon JJ, Spackman MA. CrystEngComm. 2007; 9:728–731.
41. Cruz-Cabeza AJ, Day GM, Motherwell WDS, Jones W. Chem. Commun. 2007:1600–1602.
42. Kofler A, Kolsek J. Mikrochim. Acta. 1969:408–435.
43. Allen FH. Acta Crystallogr., Sect. B. 2002; 58:380–388. [PubMed: 12037359]
44. Tai XS, Xu J, Feng YM, Liang ZP. Acta Crystallogr., Sect. E: Struct. Rep. Online. 2008; 64:o1026, o1026–1-o1026, o1026–6.
45. Krishnakumar V, Xavier RJ. Chem. Phys. 2005; 312:227–240.
46. Arjunan V, Saravanan I, Ravindran P, Mohan S. Spectrochim. Acta, Part A. 2009; 74A:375–384.
47. Gu CH, Li H, Gandhi RB, Raghavan K. Int. J. Pharm. 2004; 283:117–125. [PubMed: 15363508]
48. Coles SJ, Gale PA. Chem. Sci. 2012; 3:683–689.
49. Oxford Diffraction Oxford Diffraction Ltd. Abingdon, Oxford, England: 2003.
50. Burla MC, Caliandro R, Camalli M, Carrozzini B, Cascarano GL, Giacovazzo C, Mallamo M, Mazzone A, Polidori G, Spagna R. J. Appl. Crystallogr. 2012; 45:357–361.
51. Sheldrick GM. Acta Crystallogr., Sect. A. 2008; 64:112–122. [PubMed: 18156677]
52. Farrugia LJ. J. Appl. Crystallogr. 2012; 45:849–854.
53. Frisch, MJ.; Trucks, GW.; Schlegel, HB.; Scuseria, GE.; Robb, JMA.; Cheeseman, R.; Scalmani, G.; Barone, V.; Mennucci, B.; Petersson, GA.; Nakatsuji, H.; Caricato, M.; Li, X.; Hratchian, HP.; Izmaylov, AF.; Bloino, J.; Zheng, G.; Sonnenberg, JL.; Hada, M.; Ehara, M.; Toyota, K.; Fukuda, R.; Hasegawa, J.; Ishida, M.; Nakajima, T.; Honda, Y.; Kitao, O.; Nakai, H.; Vreven, T.; Montgomery, JA.; Peralta, JE.; Ogliaro, F.; Bearpark, M.; Heyd, JJ.; Brothers, E.; Kudin, KN.; Staroverov, VN.; Kobayashi, R.; Normand, J.; Raghavachari, K.; Rendell, A.; Burant, JC.; Iyengar, SS.; Tomasi, J.; Cossi, M.; Rega, N.; Millam, JM.; Klene, M.; Knox, JE.; Cross, JB.; Bakken, V.; Adamo, C.; Jaramillo, J.; Gomperts, R.; Stratmann, RE.; Yazyev, O.; Austin, AJ.; Cammi, R.; Pomelli, C.; Ochterski, JW.; Martin, RL.; Morokuma, K.; Zakrzewski, VG.; Voth, GA.; Salvador, P.; Dannenberg, JJ.; Dapprich, S.; Daniels, AD.; Farkas; Foresman, JB.; Ortiz, JV.; Cioslowski, J.; Fox, DJ. Gaussian 09. Gaussian Inc.; Wallingford CT: 2009.
54. Karamertzanis PG, Pantelides CC. J Comput Chem. 2005; 26:304–324. [PubMed: 15622548]
55. Karamertzanis PG, Pantelides CC. Mol. Phys. 2007; 105:273–291.
56. Habgood M, Sugden I, Kazantsev AV, Adjiman CS, Pantelides CC. JCTC. 2015 (accepted).
57. Coombes DS, Price SL, Willock DJ, Leslie M. J. Phys. Chem. 1996; 100:7352–7360.
58. Breneman CM, Wiberg KB. J. Comput. Chem. 1990; 11:361–373.
59. Price SL, Leslie M, Welch GWA, Habgood M, Price LS, Karamertzanis PG, Day GM. Phys. Chem. Chem. Phys. 2010; 12:8478–8490. [PubMed: 20607186]
60. Stone AJ. J. Chem. Theory Comput. 2005; 1:1128–1132. [PubMed: 26631656]
61. Stone, AJ. GDMA: A Program for Performing Distributed Multipole Analysis of Wave Functions Calculated Using the Gaussian Program System [2.2]. University of Cambridge Cambridge; United Kingdom: 2010.
62. Kazantsev AV, Karamertzanis PG, Adjiman CS, Pantelides CC. J. Chem. Theory Comput. 2011; 7:1998–2016. [PubMed: 26596459]
63. Clark SJ, Segall MD, Pickard CJ, Hasnip PJ, Probert MJ, Refson K, Payne MC. Z. Kristallogr. 2005; 220:567–570.
64. Perdew JP, Burke K, Ernzerhof M. Phys. Rev. Lett. 1996; 77:3865–3868. [PubMed: 10062328]
65. Vanderbilt D. Phys. Rev. B. 1990; 41:7892–7895.
66. Tkatchenko A, Scheffler M. Phys. Rev. Lett. 2009; 102:073005-1–073005/4. [PubMed: 19257665]
67. Grimme S. J. Comput. Chem. 2006; 27:1787–1799. [PubMed: 16955487]

68. Gavezzotti A. New J. Chem. 2011; 35:1360–1368.
69. Gavezzotti A. J. Phys. Chem. B. 2002; 106:4145–4154.
70. Gavezzotti A. J. Phys. Chem. B. 2003; 107:2344–2353.
71. Etter MC, MacDonald JC, Bernstein J. Acta Crystallogr., Sect. B. 1990; 46:256–262. [PubMed: 2344397]
72. Braun DE, Gelbrich T, Kahlenberg V, Laus G, Wieser J, Griesser UJ. New J. Chem. 2008; 32:1677–1685.
73. Spackman MA, Jayatilaka D. CrystEngComm. 2009; 11:19–32.
74. Wolff, SK.; Grimwood, DJ.; McKinnon, JJ.; Turner, MJ.; Jayatilaka, D.; Spackman, MA. CrystalExplorer [3.1]. University of Western Australia; Perth: 2012.
75. Markvardsen AJ, David WIF, Johnson JC, Shankland K. Acta Crystallogr., Sect. A. 2001; 57:47–54. [PubMed: 11124502]
76. David WIF, Shankland K, van de Streek J, Pidcock E, Motherwell WDS, Cole JC. J. Appl. Crystallogr. 2006; 39:910–915.
77. Coelho, AA. Topas Academic V5 Version 5 Coelho Software Brisbane. 2012.
78. Kuhnert-Brandstaetter M, Proell F. Mikrochim. Acta. 1983; 3:287–300.
79. Burger A, Ramberger R. Mikrochim. Acta. 1979; 2:273–316.
80. Florence AJ, Johnston A, Price SL, Nowell H, Kennedy AR, Shankland N. J. Pharm. Sci. 2006; 95:1918–1930. [PubMed: 16850425]
81. Cruz-Cabeza AJ, Day GM, Motherwell WDS, Jones W. Cryst. Growth Des. 2006; 6:1858–1866.
82. Schinzer WC, Bergren MS, Aldrich DS, Chao RS, Dunn MJ, Jeganathan A, Madden LM. J. Pharm. Sci. 1997; 86:1426–1431. [PubMed: 9423158]
83. Braun DE, Kahlenberg V, Gelbrich T, Ludescher J, Griesser UJ. CrystEngComm. 2008; 10:1617–1625.
84. Schmidt AC, Niederwanger V, Griesser UJ. J. Therm. Anal. Calorim. 2004; 77:639–652.
85. Berzins A, Skarbulis E, Rekis T, Actins A. Cryst. Growth Des. 2014; 14:2654–2664.
86. Gelbrich T, Threlfall TL, Hursthouse MB. CrystEngComm. 2012; 14:5454–5464.

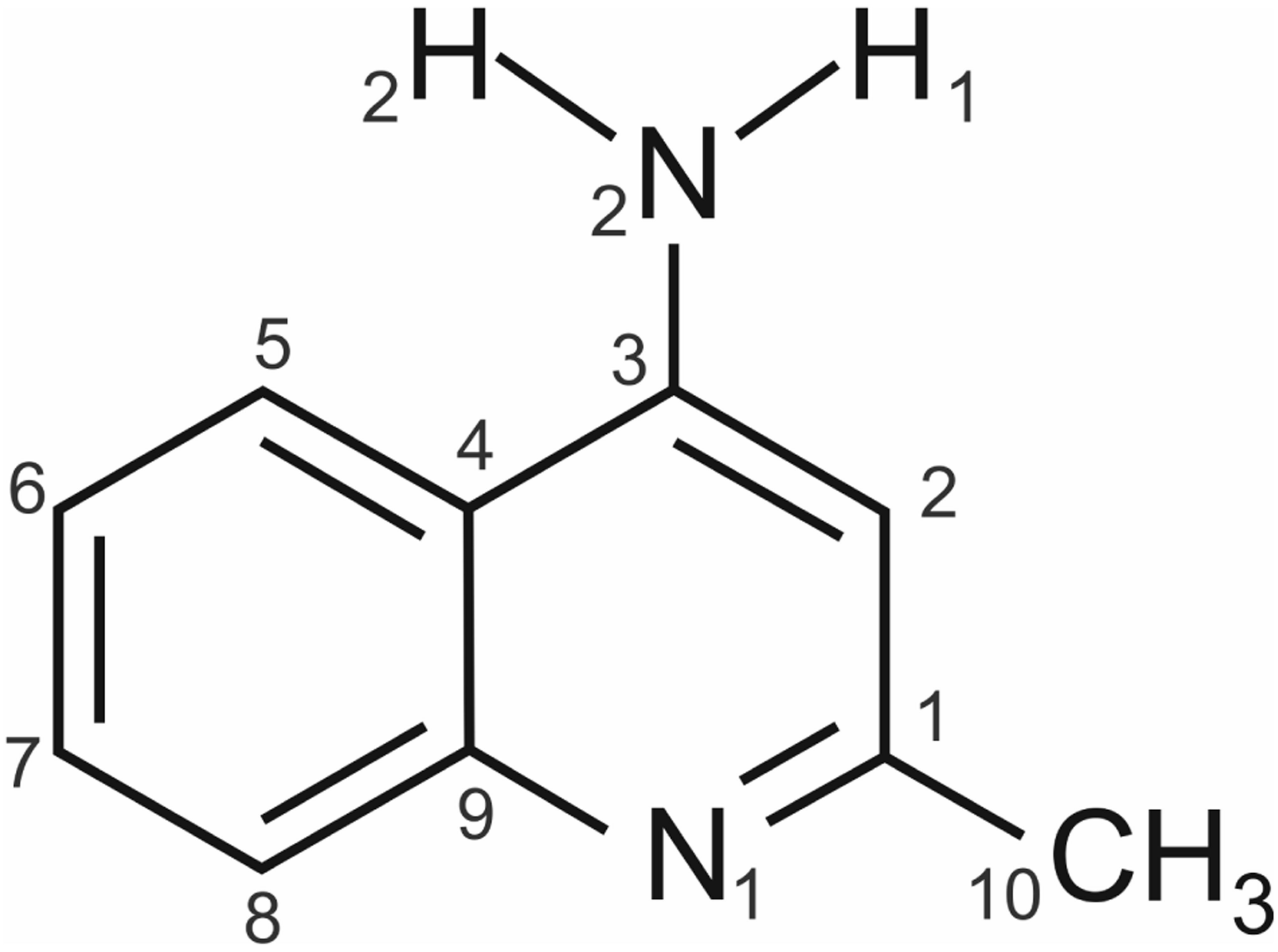

Fig. 1.
Molecular diagram of 4-amino-2-methylquinolidine (4-aminoquinaldine).

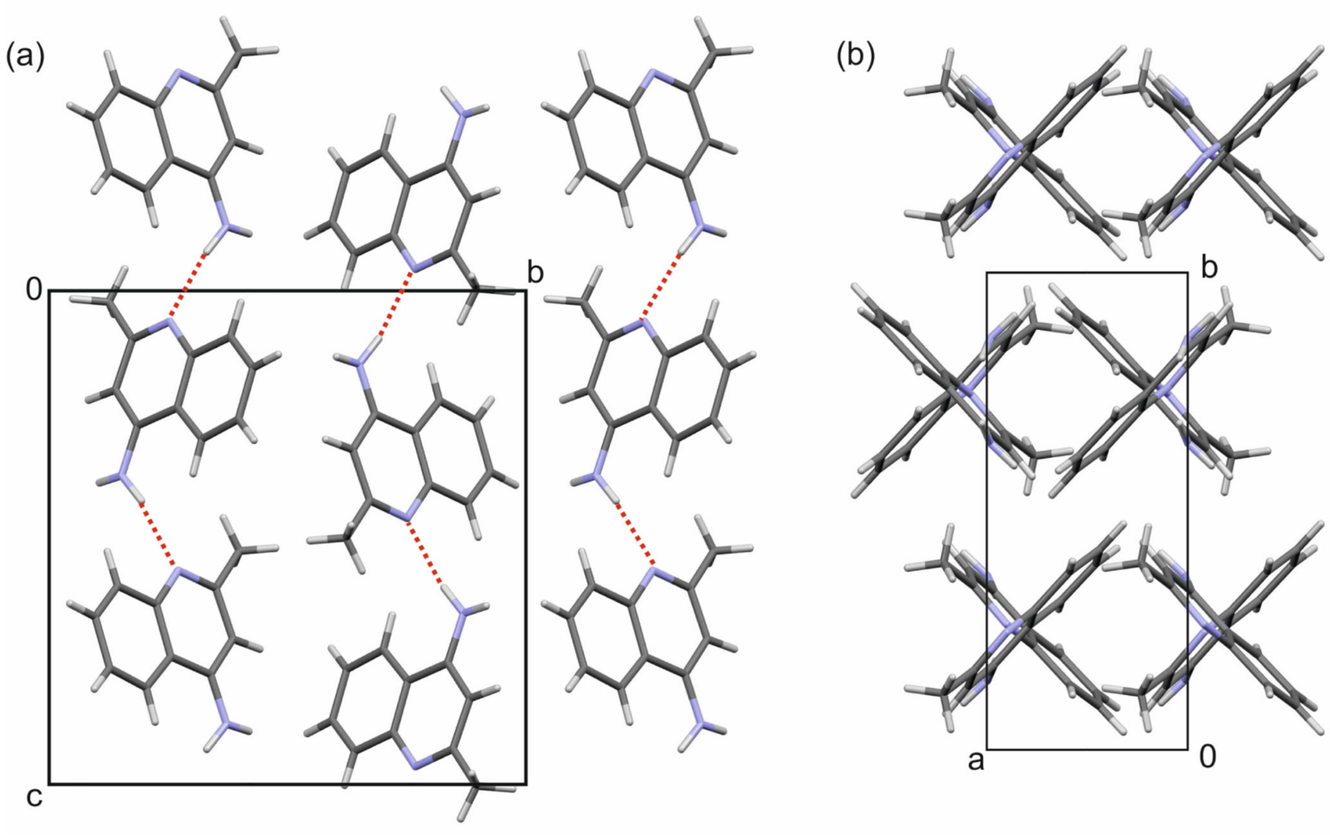

Fig. 2.

(a,b) Packing and hydrogen bonding motif present in **4-AQ AH I°**. Hydrogen bonds shown as red dotted lines in (a). Only one orientation of the disordered – CH_3 group shown.

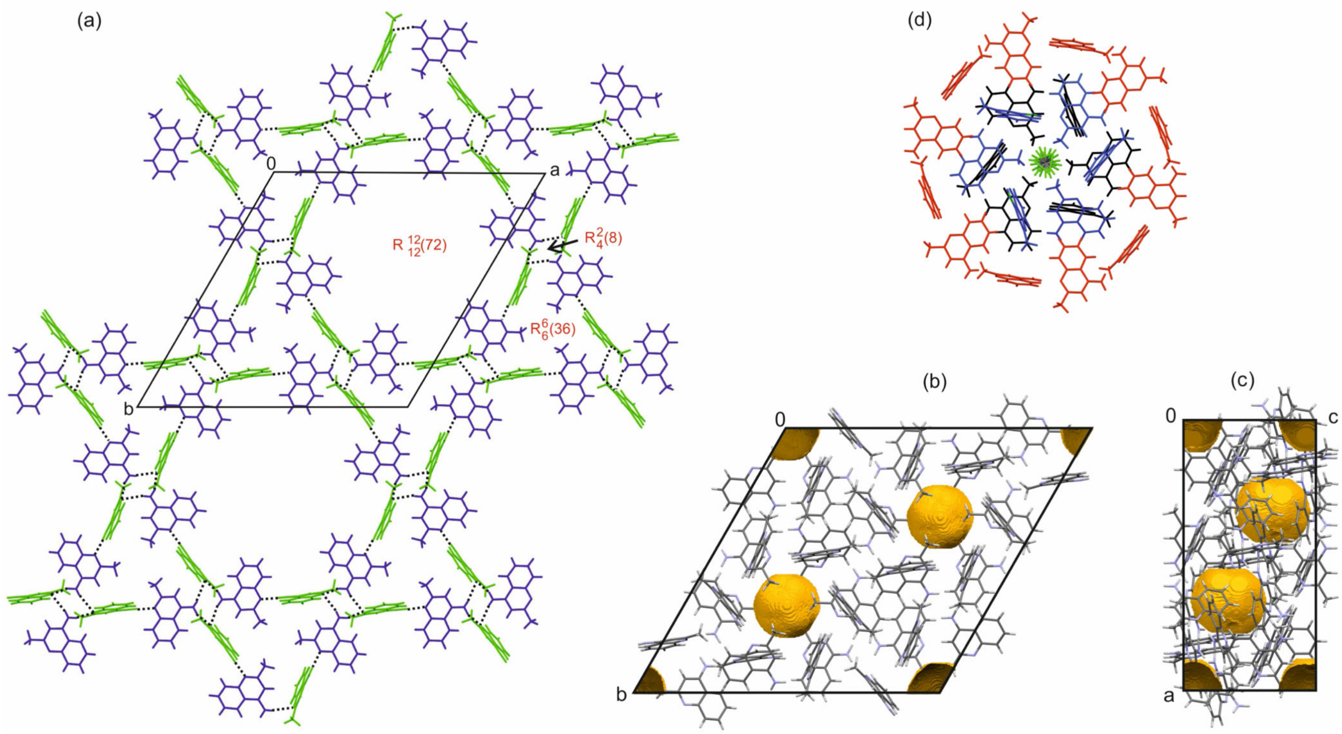

Fig. 3.

Packing and hydrogen bonding motifs of **4-AQ AH II**: (a) Graph set notation and hydrogen bonds shown in red and as black dotted lines, respectively. Symmetry independent **4-AQ** molecules are coloured differently: blue – molecules A and green – molecules B. (b, c) Unit cell and voids visualisation (2.0 Å probe radius) of the “solvent stripped” **AH II** (CCl_4) structure. The yellow surfaces represent the boundaries of calculated voids in the structure and correspond to the location of the CCl_4 molecule (c) in **AH II** (CCl_4). Disorder of –CH3 group for clarity not shown. (d) Stacked $R_{12}^{12}(72)$ and $R_6^6(36)$ ring motifs with disordered CCl_4 in the centre. Note that the **4-AQ** molecules involved in the same ring motif are coded in one colour.

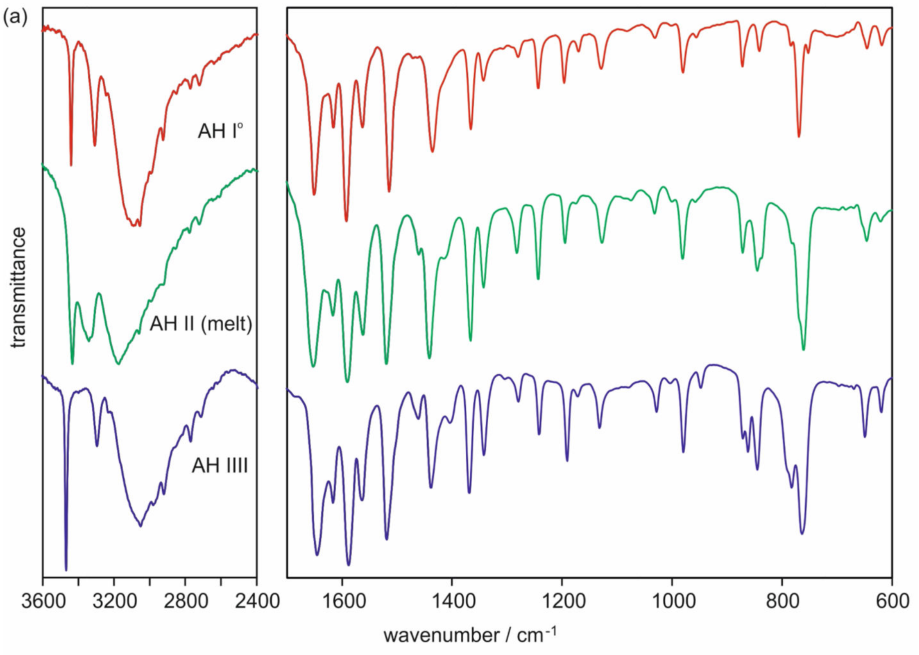

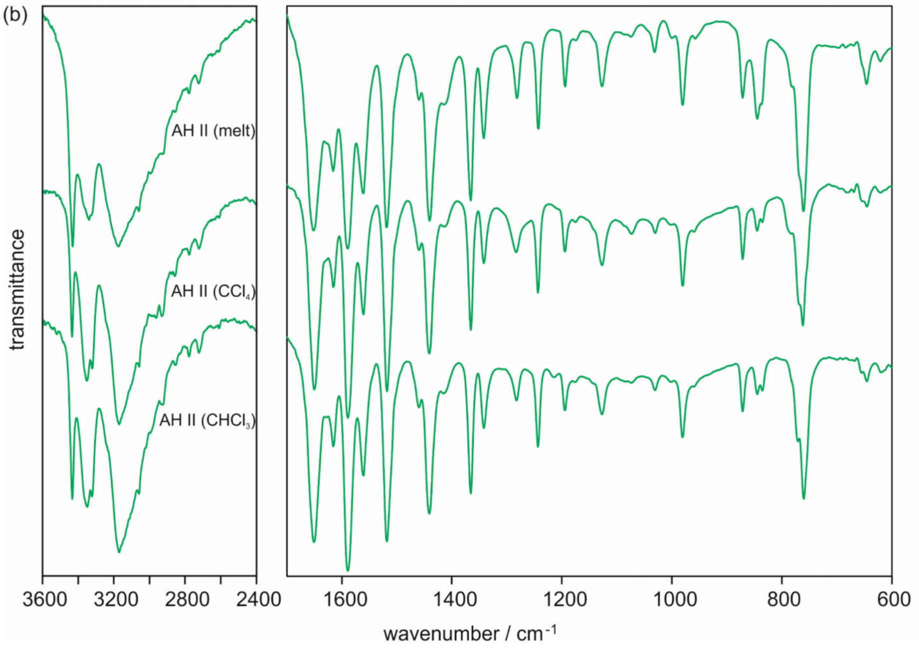

Fig. 4.

FT-IR spectra of (a) the **4-AQ** anhydrates and (b) **4-AQ AH II** samples crystallised from the melt or solvents (carbon tetrachloride or chloroform).

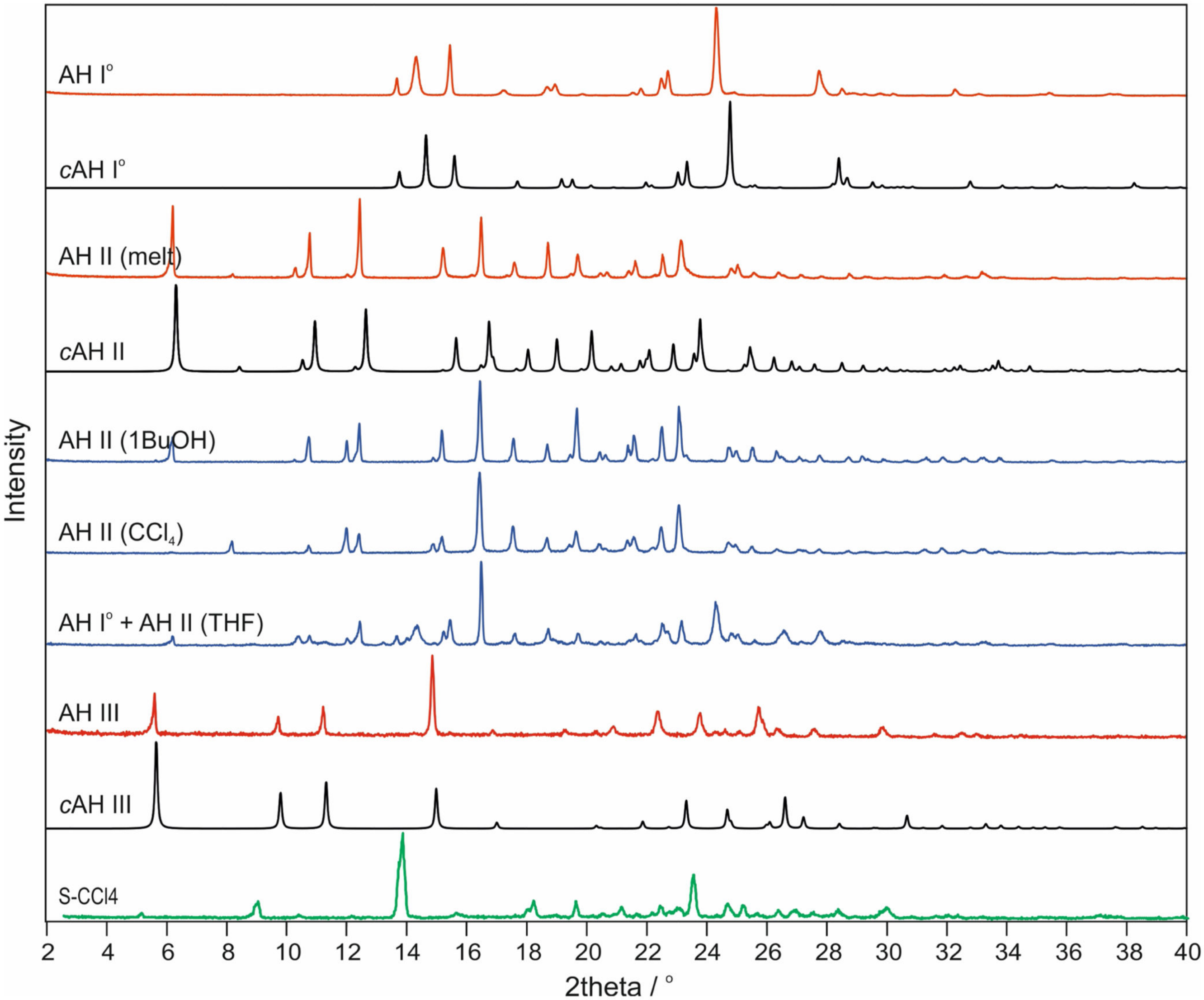

Fig. 5.

Experimental X-ray powder diffraction patterns (**AH I°**, **AH II**, **AH III**, **S**$_{\mathbf{CCl4}}$) obtained at room temperature compared with simulated patterns (λ = 1.5418 Å) for computationally generated anhydrate structures (Section 3.5). For **AH II** data for samples obtained from different crystallisation experiments are shown.

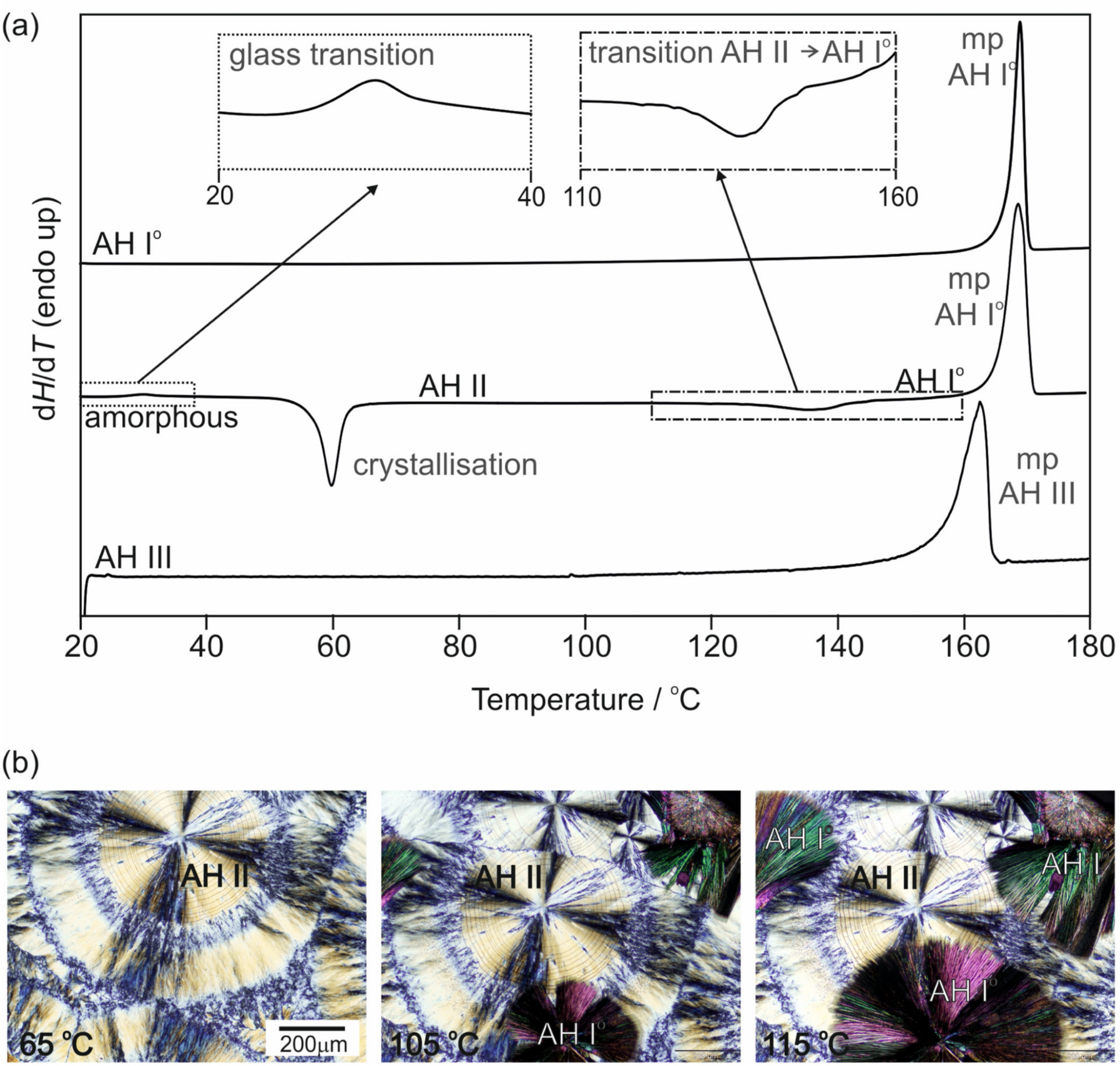

Fig. 6.

(a) DSC curves (heating rate 10 °C min^{-1}) of **4-AQ** anhydrate polymorphs; mp – melting point. The inserts show the glass transition and **AH II** → **AH I°** phase transformation. (b) Microphotographs showing the **AH II** → **AH I°** phase transformation in the temperature range 105 to 115 °C.

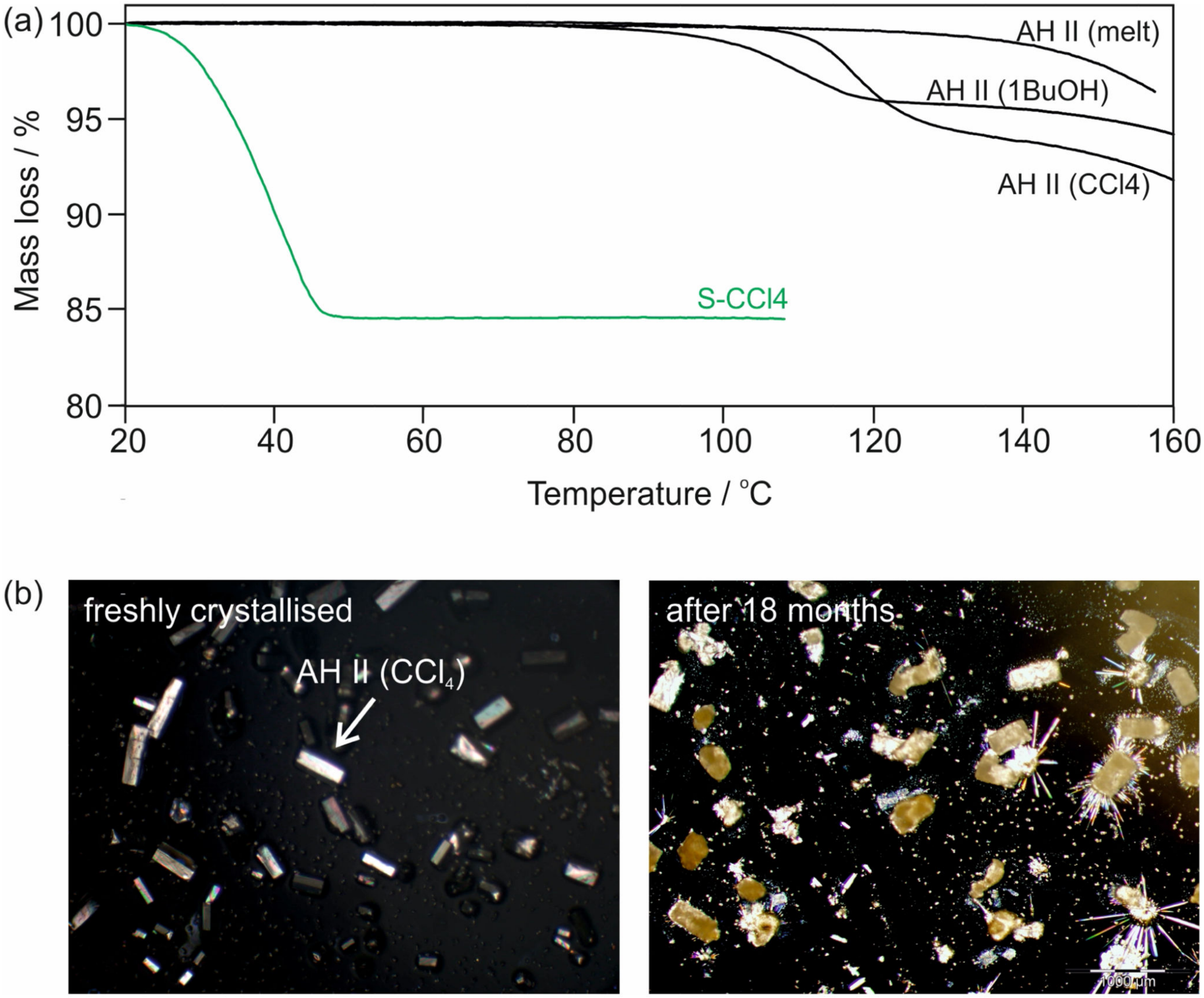

Fig. 7.

(a) TGA curves (heating rate 5 °C min^{-1}) of **4-AQ AH II** crystallised from the melt, 1-butanol or carbon tetrachloride and **S_{CCl4}**. (b) Microphotographs of (left) freshly crystallised **AH II** from carbon tetrachloride and (right) of the same sample stored for 18 months at ambient conditions. The elongated plates (**AH I°**) grown on top of the crystals of the stored sample formed due to sublimation.

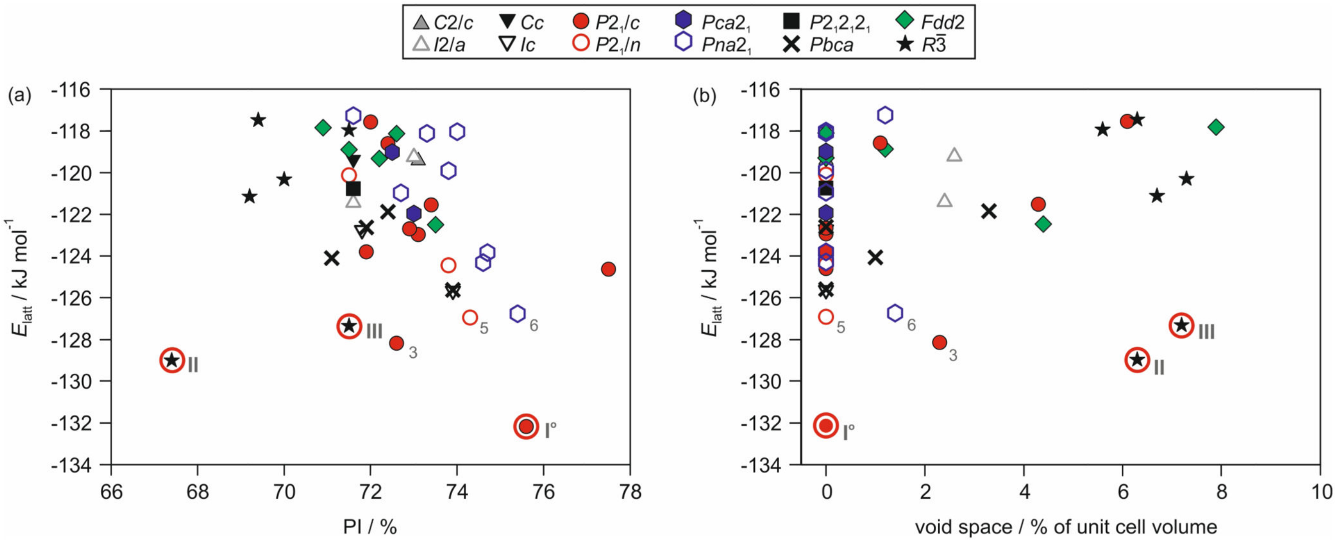

Fig. 8.

Crystal energy landscape for **4-AQ** anhydrates, classified by space group. Each symbol denotes a crystal structure. Experimental structures are encircled and labelled with Roman numbers. Arabic numbers are used for the most stable hypothetical structures and the numbers correspond to their stability rank (ESI† Table S6). In (a) the packing index (PI) and in (b) the void space calculated using a 1.0 Å probe radius are plotted against lattice energies (E_{latt}).

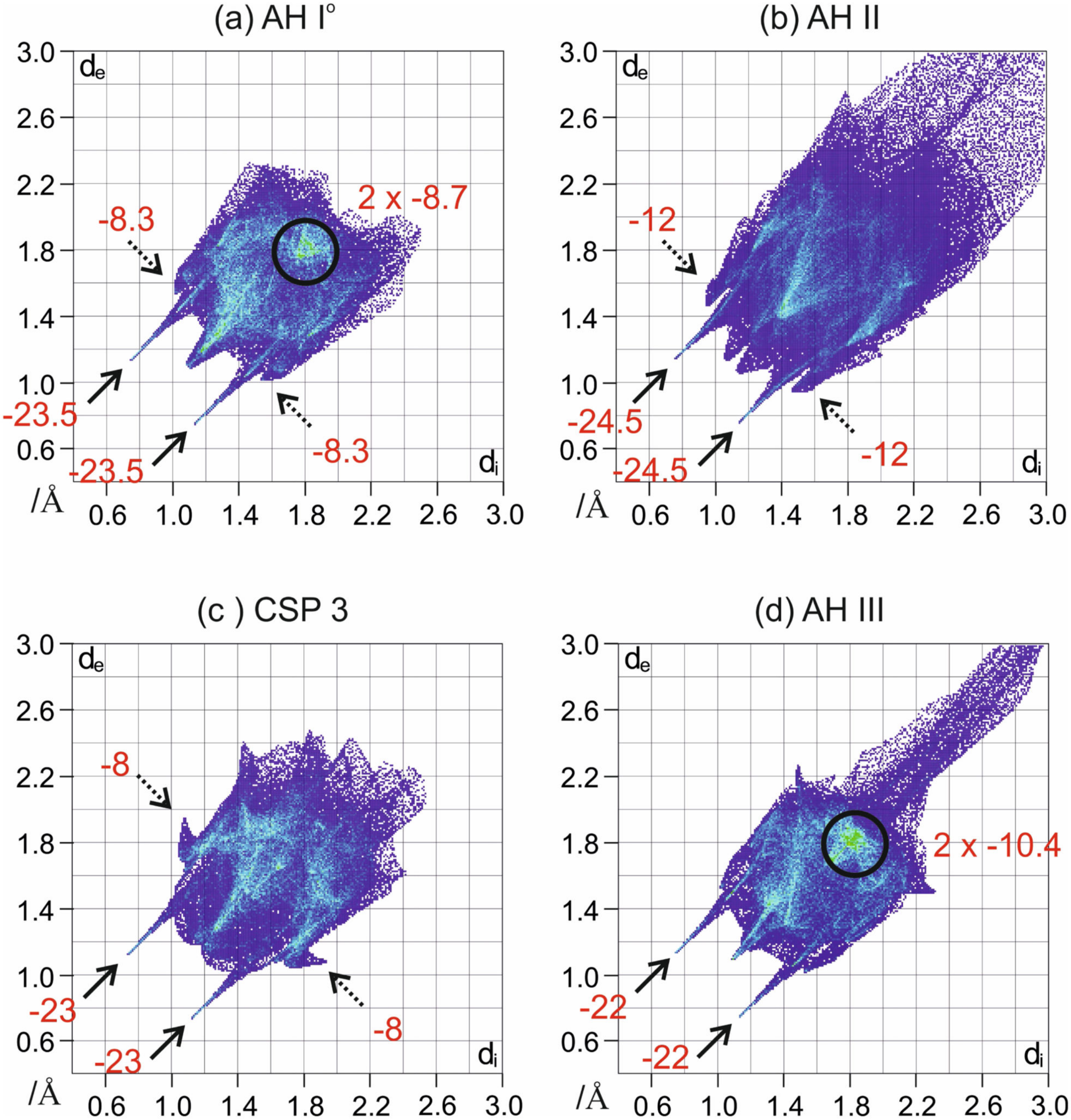

Fig. 9.

2D Fingerprint plots derived from Hirshfeld surfaces[73,74] of (a) **4-AQ AH I°**, (b) **AH II**, (c) third lowest energy structure on **Error! Reference source not found.** and (d) **AH III** (rank 4 structure). The large number of points at high values of d_e and d_i in (b) and (d) are indicative of voids in the structures. Numbers correspond to PIXEL[68-70] energies of the strongest intermolecular interactions (ESI† Table S8), with N–H⋯N hydrogen bonds indicated with solid arrows, C–H⋯πC short contacts with dotted arrows and the regions of π⋯π interactions encircled.

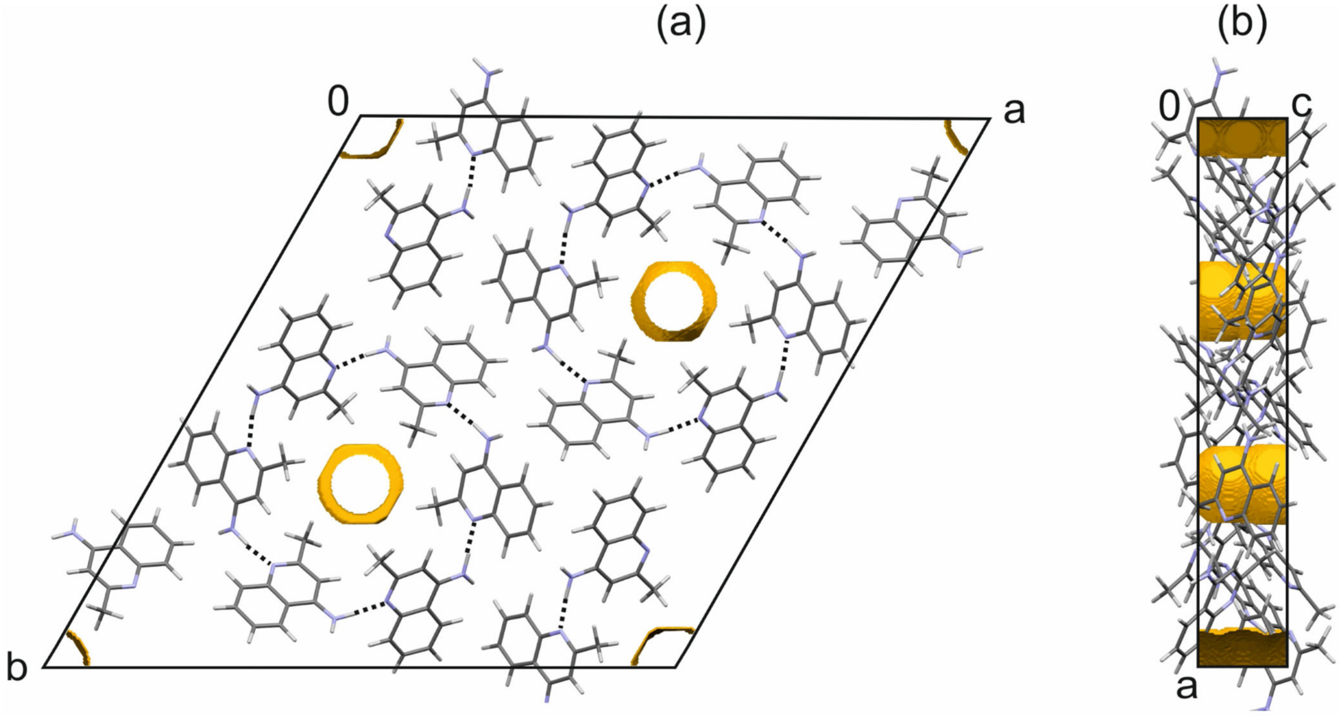

Fig. 10.

(a) Hydrogen bonding and (a,b) unit cell and voids visualisation (2.0 Å probe radius) of the computationally generated **AH III** structure. The yellow surfaces represent the boundaries of calculated voids in the structure.

Table 1

Crystal data and structure refinement details.

Compound	**AH I°**	**AH II (CCl_4)**
Chemical formula	$C_{10}H_{10}N_2$	$C_{10}H_{10}N_2 \cdot 0.085\ (CCl_4)$
M /g mol^{-}1	158.20	342.03
Crystal system	monoclinic	trigonal
Space group	$P2_{1/c}$	$R\bar{3}$
Z/Z'	4/1	18/2
a/Å	5.2162(4)	28.4074(8)
b/Å	12.3693(9)	
c/Å	13.1192(9)	11.9126(5)
β/°	99.065(3)	
Unit cel volume /Å^3	835.89(11)	8325.3(6)
Temperature / K	293(2)	173(2)
Density / g cm^{-3}	1.257	1.228
No. of reflections measured	4759	11536
No. of independent ref.	1502	3315
R_{int}	0.027	0.032
Parameters	128	275
Final R_1 values ($I > 2\sigma(I)$)	0.037	0.056
Final $wR(F^2)$ values (all data)	0.106	0.164
CCDC no.	1043184	1043185

Table 2

Selected FT-IR band positions for **4-AQ** anhydrates.

	AH I°	**AH II (melt)**[a]	**AH II (CCl_4)**[a]	**AH II ($CHCl_3$)**[a]	**AH III**
$\nu\mathrm{NH_2}$	3438	3431	3434	3433	3466
	3307	3339/	3352/	3349/	3294
		3329	3322	3323	
νCH,		3170/	3171/	3170/	
$\nu\mathrm{CH_3}$	3055/	3060/	3058/	3058/	3051/
	2994/	2993/	2995/	2996/	2981/
	2925	2923	2929	2931	2921
$\delta\mathrm{NH_2}$	1650	1652	1650	1651	1645
νC=C	1615	1616	1615	1616	1616
	1562	1561	1561	1561	1563
	1514	1519	1518	1518	1518
νC=N	1592	1590	1589	1589	1587
$\delta\mathrm{CH_3}$	1435	1440	1441	1441	1438

[a] For **AH II** three different crystallisation products are compared, i.e. crystallisation from the melt, carbon tetrachloride and chloroform.

Table 3

Physicochemical data for **4-AQ** polymorphs.

Modification	**AH I°**	**AH II (melt)**	**AH III**
T_{fus} / °C[a]			
HSM	167		156 – 157.5
DSC (onset) ± 95 c.i.	167.3 ± 0.1		157.1 ± 0.3
$\Delta_{fus}H$[b] ± 95 c.i. / kJ mol^{-1}	25.4 ± 0.1	22.1 ± 0.2[f]	20.0 ± 0.5
T_{trs}[c] / °C			
HSM		100 – 140	
DSC (onset) ± 95 c.i.		116 ± 3	
$\Delta_{trs}H$[d] to AH I° ± 95 c.i. / kJ mol^{-1}		−3.3 ± 0.1	−5.4 ± 0.6[g]
E_{latt} / kJ mol^{-1} (PBE-G06)	−132.18	−129.00	−127.35
Order of thermodynamic stability			
DSC	a (highest)	b	c
E_{latt}, −273 °C	a (highest)	b	c
density order[e]	a (highest)	c	b

[a] temperature of fusion,

[b] heat of fusion,

[c] transition temperature,

[d] heat of transition,

[e] derived from computationally generated structures (see Section 3.5) and indexing of XRPD patterns (ESI† Table S7),

[f] calculated: sum of $\Delta_{fus}H_{I°}$ and $\Delta_{trs}H_{II\text{-}I°}$,

[g] calculated: difference $\Delta_{fus}H_{III}$ and $\Delta_{fus}H_{I°}$.